Phasing the Primary Mirror Segments of the Keck Telescopes: A Comparison of Different Techniques

Gary Chanan[a], Mitchell Troy[b], and Catherine Ohara[a]

[a]University of California, Irvine, Department of Physics and Astronomy, Irvine, CA 92697
[b]Jet Propulsion Laboratory, California Institute of Technology, Pasadena, CA 91109

ABSTRACT

We have developed and tested extensively three different methods for phasing the primary mirror segments of the Keck telescopes. Two of these, referred to as the broadband and narrowband algorithms respectively, are physical optics generalizations of the Shack-Hartmann technique. The third, Phase Discontinuity Sensing (PDS), is a physical optics generalization of curvature sensing. We evaluate and compare experimental results with these techniques with regard to capture range (as large as 30 μm), run-to-run variation (as small as 6 nm), execution time (as short as twenty minutes), systematic errors, ease of implementation, and other factors, in the context of the Keck telescopes and also of future very large ground-based telescopes.

Keywords: phasing, segmented mirrors, telescopes

1. INTRODUCTION

In addition to being the largest optical and infrared telescopes in the world, the Keck telescopes are also extremely valuable as test beds for the development of key technologies needed for segmented telescopes of the future, such as the Next Generation Space Telescope,[1] or the proposed extremely large ground based telescopes such as the California Extremely Large Telescope (CELT)[2] and OWL.[3] In particular, we have used the Kecks to develop techniques for phasing segmented mirrors, i.e. wavefront sensing on piecewise discontinuous wavefronts. In this work we describe and compare three such phasing techniques.

The importance of proper phasing to segmented telescopes can scarcely be overstated. At wavelengths that are long enough that the full aperture is in principle diffraction limited (or for space-based applications), the resolution of a perfectly phased telescope is better by a factor of $\sqrt{n}$ (where n is the number of segments) than the resolution of the corresponding completely unphased telescope. [For CELT, with a proposed 1098 segments, this is a factor of 33.] Even for imaging through the turbulent atmosphere, phasing can have an enormous impact. Figure 1 shows theoretical point spread functions for the Keck telescope[4] as a function of wavelength and rms phase error (measured at the surface, not at the wavefront). While phasing makes little difference at a wavelength of 0.5 μm, even a phase error of 100 nm begins to have an effect at a wavelength of 2 μm. If the atmosphere is not present (as for NGST) or if its effects are canceled out by an adaptive optics system, then even phase errors of 25 nm at 1 μm can have a significant effect on the telescope modulation transfer function.[5,6]

This paper is organized as follows. In Section 2 we describe the three techniques qualitatively. In Section 3 we present a brief overview of the theory underlying each technique. In Section 4 we summarize the experimental results obtained with the three techniques and give a quantitative comparison. Finally, in Section 5 we consider the application of these techniques to the telescopes of the future.

2. QUALITATIVE COMPARISON OF THE THREE METHODS

In all phasing algorithms under consideration in this paper, we assume that the segments have first been aligned in tip and tilt to a high degree of accuracy - small enough that any remaining tip/tilt errors are not the dominant contributor to the phasing residuals. At Keck we attain a tip/tilt accuracy of order ± 0.02 arcseconds (one dimension, rms), and have shown that the phasing residuals are then dominated by segment aberrations.[4,7] Phase errors are quoted throughout as surface errors, not wavefront errors (which would be a factor of two larger).

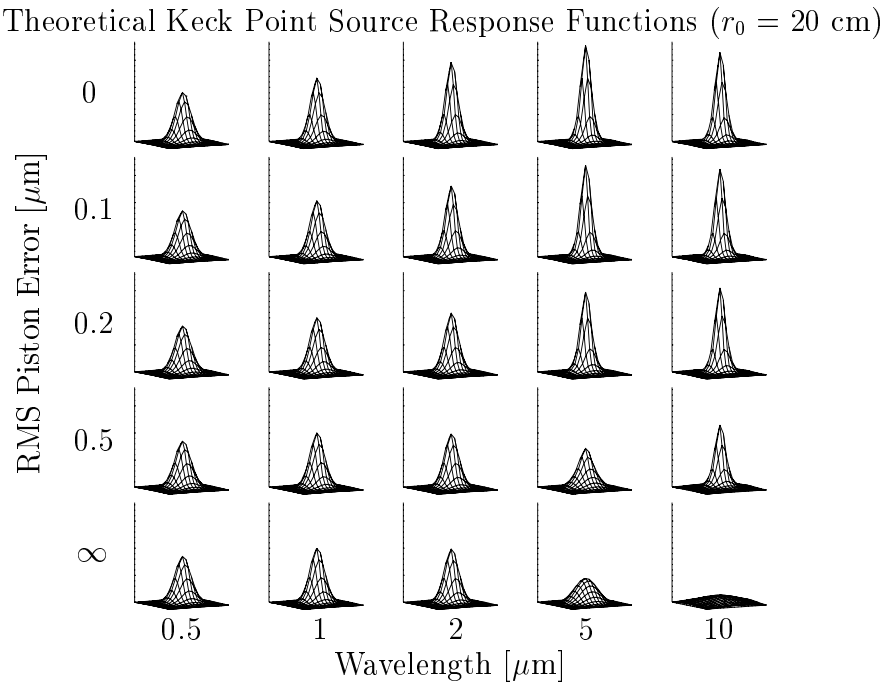

Figure 1. Theoretical point response functions for the Keck telescopes, assuming an atmospheric coherence diameter of $r_0(0.5\ \mu\text{m}) = 20$ cm, for a variety of wavelengths and piston errors of the primary mirror segments. The profiles have been averaged over an ensemble of configurations which are consistent with the given RMS piston error. All plots are to the same scale. FWHM of the images is 0.5 arcseconds at $\lambda = 0.5\ \mu$m. Note the devastating effects of phase errors at the longer wavelengths.

2.1. Narrowband Shack-Hartmann Phasing

In this algorithm, the primary mirror is re-imaged at small magnification (1:200) and a mask is placed over the re-imaged pupil as in the usual geometrical optics Shack-Hartmann test.[8] In this case however, the Hartmann apertures are all centered on the midpoints of the intersegment edges, so that they each straddle two adjacent segments (see Figure 2). An array of microprisms and a single objective lens directs the resulting stellar subimages to different positions on the detector. [This rather specialized optic was selected instead of the usual Shack-Hartmann microlens array for reasons of image quality,[9] but this substitution no longer appears to be necessary (see below).]

The two discrete halves of each Hartmann subaperture can now be thought of as the two slits in a Young's experiment. Phase differences between the two halves manifest themselves in the resulting diffraction patterns on the detector, and these phase relationships can be extracted by cross-correlation techniques.

Because the diffraction patterns are a periodic function of the phase difference between the two segments, this algorithm has a highly non-linear response. In principle, the "capture range" of the algorithm (i.e. the maximum piston error which can be reliably detected) should be about $\pm\lambda/4$ or about ± 225 nm for our 900 nm operating wavelength. However because of the need to stay well away from the dangerously non-linear response region, in practice the capture range is not much more than ± 100 nm.

The principal disadvantages of the method are the specialized instrumentation required, the non-linear response, and the associated small capture range. In addition, since the re-imaged pupil needs to be well-aligned with the mask, a careful pupil-registration step is required. Finally, the method utilizes only a small fraction of the segment surface. Technically the algorithm minimizes not the overall wavefront error but the intersegment edge steps; for badly aberrated segments, there can be substantial differences between these two minimizations. The advantages of the method are its speed - once the pupil is properly registered, only a single 30 to 60 second exposure on a star is needed - and its accuracy, which we have recently shown to be 6 nm.

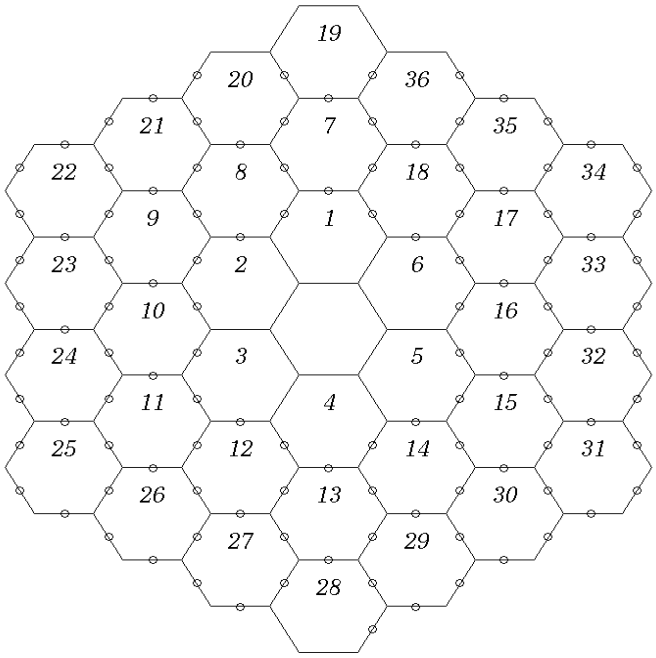

Figure 2. The geometry of the primary mirror of the Keck telescopes, showing the 78 circular subapertures which sample the intersegment edges in the phasing procedure. Each segment is 0.9 meters on a side. The subapertures are 12 cm in diameter. The 35 peripheral subapertures are used for pupil registration.

2.2. Broadband Shack-Hartmann Phasing

The broadband algorithm is similar to the narrowband and uses identical hardware, but it exploits the finite bandwidth of the filters which define the wavelength of the starlight. The signal is the degree of coherence of the subimage, and the relevant scale is not the wavelength but the coherence length of the filter.[4] This is not only in general much larger than the wavelength, but it can be tuned to the conditions at hand if one has an *a priori* estimate of the phase errors involved. As a result this technique has an enormously large capture range and also dynamic range, and it is the workhorse phasing algorithm at Keck.

This technique shares with the narrowband technique the disadvantages of special hardware and pupil registration requirements; it also minimizes intersegment edge steps, not overall wavefront error. In the Keck implementation, the use of microprisms causes another complication as dispersion in these prisms introduces a spurious source of incoherence which must be taken out in software[4]; however, if microlenses were used, this would not be a problem. This technique is also somewhat time consuming in that it requires multiple exposures in order to trace out the coherence curves which ultimately provide the phase information. Depending on the initial phase errors, the full procedure can take up to 90 minutes. Advantages are not only the large capture range and dynamic range, but the inherent stability of the method, since the response curves are Gaussian, and not periodic as in the case of the narrowband method.

2.3. Phase Discontinuity Sensing

Phase discontinuity sensing[10] is the wave optics generalization of curvature sensing.[11–13] It has the immediate advantage that no special purpose hardware is required, only an infrared area detector of suitable image scale. As with curvature sensing, this technique extracts wavefront information from out of focus images, but one uses long wavelengths (3 μm) and a restriction to small piston errors ($\pm$400 nm) essentially to linearize the problem. Since the linearization is only approximate, the technique is iterative and requires multiple exposures; in addition one does not solve for the phase errors explicitly, rather one drives them to zero.

Advantages of the method are the fact that no special hardware and no pupil registration is required. In addition, it utilizes a larger fraction of the segment surface than the Shack-Hartmann techniques. The capture range is larger than that of the narrowband technique but is still limited, and the multiple exposures (both on and off source) make it more time consuming. The full procedure takes about 45 minutes.

3. BRIEF THEORETICAL DESCRIPTION OF THE THREE METHODS

3.1. Narrowband Shack-Hartmann Technique

This algorithm[14] is based upon diffraction from a single subaperture with a phase step in the middle. The diffraction pattern formed by this subaperture depends sensitively on the physical step height between the two segments. A detailed discussion may be found elsewhere.[4]

Let $\vec{\rho}$, with rectangular coordinates (ξ, η) [in units of length] or circular coordinates (ρ, θ), be the position vector in the subaperture plane and let $\vec{w}$, with rectangular coordinates (x, y) [in radians] or circular coordinates (w, ψ), be the position vector in the image plane. We consider a circular subaperture of radius a, symmetrically straddling two segments divided by the line $\eta = 0$; the upper segment ($\eta > 0$) has a piston error of $\delta/2$, and the lower segment ($\eta < 0$) has a piston error of $-\delta/2$. [Thus δ is the physical step height; the corresponding wavefront step height is 2δ.] The light is taken to be monochromatic, with wavelength λ.

In the absence of other aberrations, the complex amplitude in the image plane $\hat{f}(\vec{w}; k\delta)$ is simply the Fourier Transform of the aperture function:

$$\hat{f}(\vec{w}; k\delta) = \frac{2}{\pi a^2} \int_0^{\pi} \int_0^{a} \cos(k\delta + k\vec{\rho} \cdot \vec{w}) \ \rho \ d\rho \ d\theta \tag{1}$$

where $k = 2\pi/\lambda$ and the normalization is chosen such that the on-axis, in-phase intensity is unity. The intensity in the image plane is simply:

$$I(\vec{w}; k\delta) = \hat{f}^2(\vec{w}; k\delta) \tag{2}$$

This integral can be handled numerically by two-dimensional fast Fourier Transform techniques; however, a modest amount of analysis can make the calculation more efficient and also provides some insight into the problem.

For an arbitrary δ we have:

$$I(\vec{w}; k\delta) = \left[\cos k\delta \ \hat{f}(\vec{w}; 0) + \sin k\delta \ \hat{f}(\vec{w}; \frac{\pi}{2})\right]^2 \tag{3}$$

i.e., the Fourier amplitude can be represented as a linear combination of the in-phase ($k\delta = 0$) and maximally out-of-phase ($k\delta = \pi/2$) amplitudes:

$$\hat{f}(\vec{w}; 0) = \frac{2}{a^2} \int_0^{a} J_0(k\rho w) \ \rho \ d\rho \ = \ \frac{2J_1(kaw)}{kaw} \tag{4}$$

$$\hat{f}(\vec{w}; \frac{\pi}{2}) = \frac{2}{\pi} \int_0^{\pi} \frac{u \cos u - \sin u}{u^2} \ d\theta \tag{5}$$

where $u = kaw \cos(\theta - \psi)$.

Figure 3 shows the theoretical diffraction patterns for a sequence of eleven equally spaced values of δ from $k\delta = 0$ to $k\delta = 10\pi/11$. The phase sensitivity is clear. When the two segments are in phase, one obtains the usual circular diffraction pattern (Airy disk). As δ is increased, the original peak shifts downward, and a second diffraction peak appears near the top of the subimage. The shift of the original peak and the relative intensity of the second peak both increase with increasing δ.

The two peaks become equal at a physical step height of $\lambda/4$, corresponding to an overall path difference of $\lambda/2$ between the two halves of the circular subaperture. As δ continues to increase, the second peak continues to grow at the expense of the first until, at $\lambda/2$ (a path difference of λ), it has replaced and is indistinguishable from the original peak. As long as the piston errors are known to be smaller than $\lambda/4$ in absolute value, extraction of the phase information is straightforward.[14]

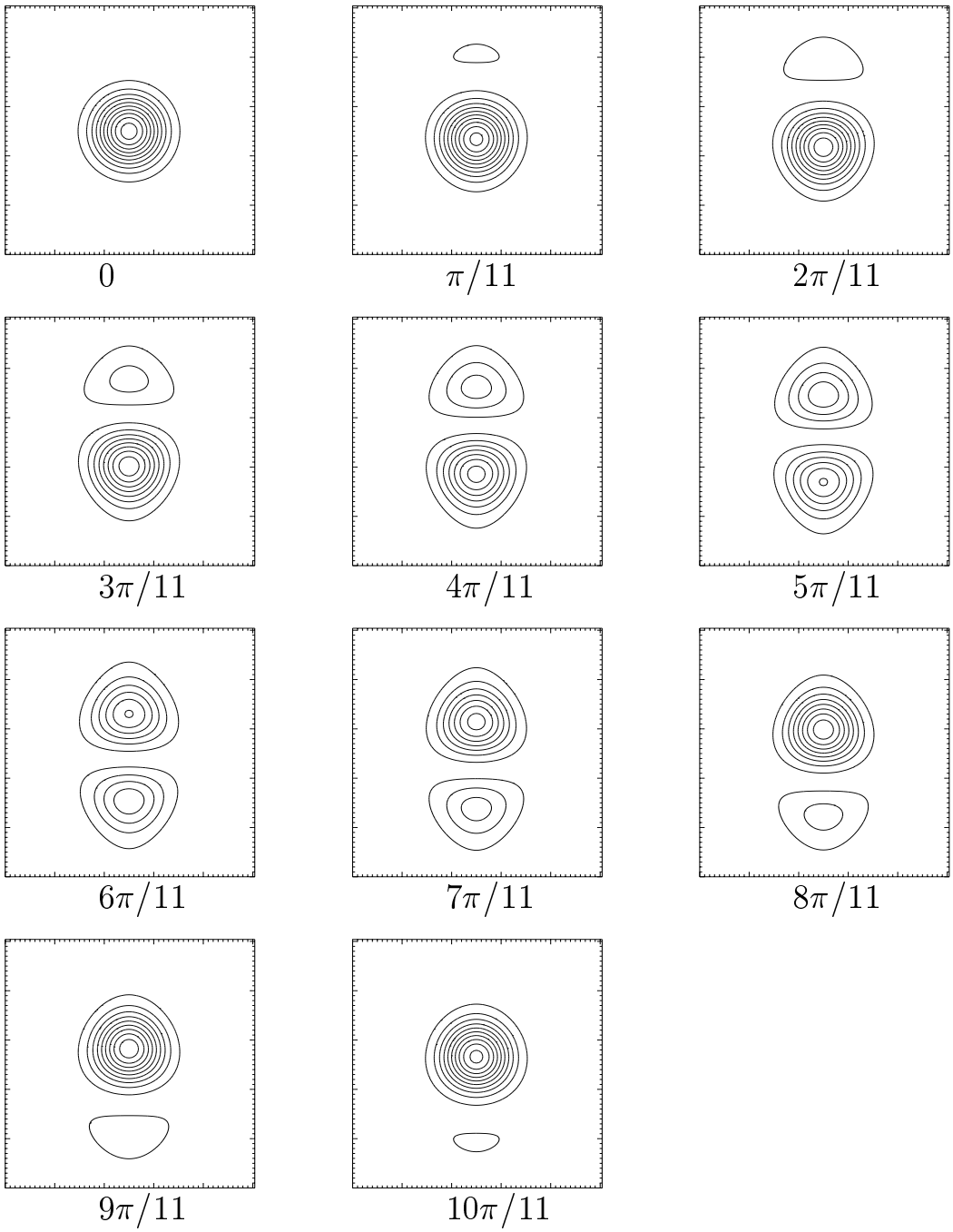

Figure 3. Theoretical diffraction patterns (monochromatic light) for a split circular subaperture of radius a with a physical step δ between the two halves given by $k\delta = 0,\ \pi/11,\ 2\pi/11, \ldots,\ 10\pi/11$. The boxes are $15/ka$ radians on a side.

3.2. Broadband Shack-Hartmann Technique

In the broadband algorithm[4] we exploit the finite wavelength interval $\Delta\lambda \approx 2\pi\Delta k/k^2$ spanned by the light; this involves integrating Eq. (3) over k. The finite spread in wavelength becomes significant for the trigonometric factor in Eq. (3) when the condition $\Delta\lambda \ll \lambda^2/2\delta$ is violated. For future reference we abbreviate $\lambda^2/2\Delta\lambda$ as l and refer to it as the coherence length. The spread in wavelength becomes significant for the $\hat{f}$ factors when the (generally

less restrictive) condition $\Delta\lambda \ll \lambda$ is violated. For simplicity here we assume $\Delta\lambda/\lambda \ll 1$, but make no assumption about the relative sizes of δ and l. This means that in integrating Eq. (3) over k, we can approximate the implicitly k-dependent $\hat{f}$ factors by evaluating them at the midpoint of the k-interval, but the $\sin k\delta$ and $\cos k\delta$ factors must be explicitly averaged over k.

We assume a Gaussian bandpass in k of variance σ_k^2. To within a constant of order of unity, σ_k is simply the reciprocal of l. The FWHM Δk is related to σ_k by $\Delta k = \sqrt{8\ln 2}\,\sigma_k$ and from the definition of l we have:

$$\sigma_k = \frac{\pi}{\sqrt{8\ln(2)}}\,\frac{1}{l} = \frac{1.334}{l} \tag{6}$$

To perform the k-averaging we multiply the right hand side of Eq. (3) by the Gaussian response of the filter and integrate over k to obtain:

$$\langle I\left(\vec{w};k\delta\right)\rangle = \alpha_1\hat{f}^2\left(\vec{w};0\right) + \alpha_2\hat{f}\left(\vec{w};0\right)\hat{f}\left(\vec{w};\frac{\pi}{2}\right) + \alpha_3\hat{f}^2\left(\vec{w};\frac{\pi}{2}\right) \tag{7}$$

where the brackets denote k-averaging and

$$\begin{aligned}
\alpha_1 &= \frac{1}{2}\left(1 + e^{-2\sigma_k^2\delta^2}\cos 2k_0\delta\right) \\
\alpha_2 &= e^{-2\sigma_k^2\delta^2}\sin 2k_0\delta \\
\alpha_3 &= \frac{1}{2}\left(1 - e^{-2\sigma_k^2\delta^2}\cos 2k_0\delta\right)
\end{aligned} \tag{8}$$

While the narrowband algorithm is based on extracting the phase (δ) information contained in the trigonometric factors of Eq. (3), the broadband algorithm is based on extracting the phase information contained in the coefficients (α_1, α_2, α_3) of Eq. (7).

To illustrate the extraction of phase information, imagine a sequence of stepped exposures analogous to that in Figure 3, except that this time we select eleven steps spanning not a half-wave, but rather roughly the coherence length l. As a specific example, consider a filter of bandwidth 10 nm and central wavelength 891 nm, corresponding to a coherence length of $l = 40$ μm. We choose a step size of 6 μm. The full range spanned by these steps is then ± 30 μm with respect to the nominal position.

A typical sequence of real CCD images generated in this manner for a particular intersegment edge is shown in Figure 4. The first and last steps of the sequence are significantly out of phase and the diffraction patterns are almost completely incoherent ($\delta \to \infty$). As we approach the middle subimages of the sequence, the patterns become more and more coherent. We emphasize that the parameter of interest is the "degree of coherence" of the subimage, not the precise value of the phase; the latter varies rapidly from subimage to subimage because of the large step size.

In order to extract phase information from a sequence of stepped subimages such as those in Figure 4, we need to quantify the notion of the degree of coherence of an individual subimage. Intuitively, the fourth through seventh subimages of Figure 4 (labeled -12μm through $+6\mu$m) have a high degree of coherence because (except for the obviously different orientation) they resemble one or another of the subimages in the "template" sequence of Figure 3. Conversely, the first and last subimages of Figure 4 bear little resemblance to any of the templates and therefore have a low degree of coherence. One can define a useful coherence parameter[4] (the detailed definition of which is beyond our scope here) which quantifies this intuitive notion and varies between 0 (for a completely incoherent subimage) and 1 (for a completely coherent one). In Figure 5 we plot this coherence parameter vs. step height for a series of numerically generated images corresponding to Eq. (7), defined by a filter of wavelength 891 nm and bandwidth 10 nm. The characteristic horizontal scale of the curve is simply the filter coherence length of $l = 40$ μm. Apart from considerable high-frequency structure, the curve can be well-approximated by a Gaussian, as shown.

In fact, in practice we simply use the Gaussian approximation; the high frequency structure is treated as noise. For our purposes it makes little difference that the origin of the noise is theoretical rather than observational. The actual coherence parameters corresponding to the diffraction patterns in Figure 4 are shown in Figure 6a. Note that unlike the narrowband algorithm, for which a single exposure is sufficient, in the broadband algorithm one must take the full sequence of eleven exposures in order to trace out the entire coherence curve and so determine its maximum.

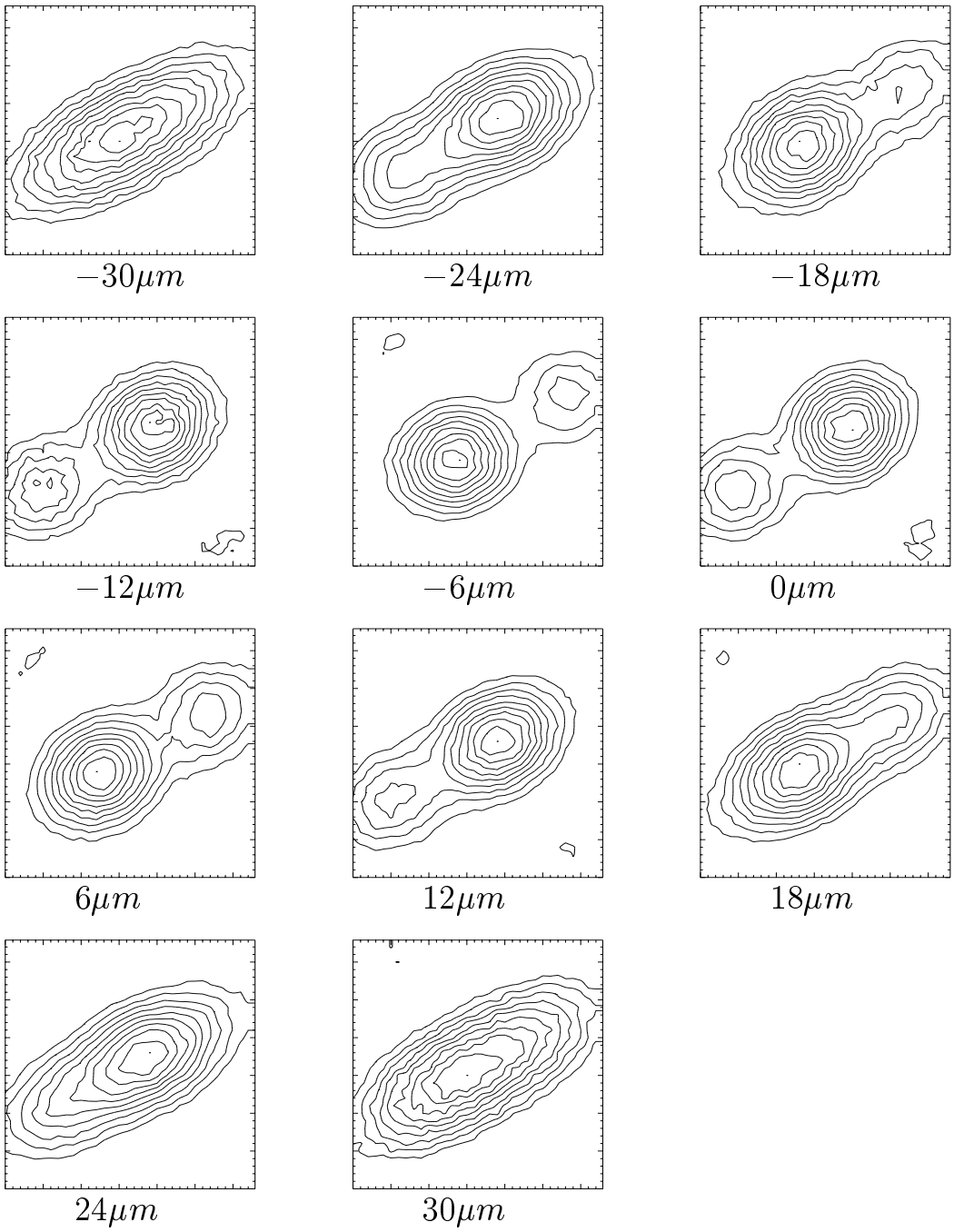

Figure 4. Typical broadband sequence of CCD subimages. Step size is 6 μm; coherence length is 40 μm. The edge is in phase between the fourth and fifth subimages [see Figure 6a]. Boxes are 5 arcseconds on a side.

Since the characteristic scale of the coherence function plotted in Figure 5 is the coherence length of the filter, we can "tune" the algorithm by selecting $\Delta\lambda$ such that l matches the expected range of piston errors for a given situation. These different coherence lengths define different modes of broadband phasing. The accuracy of a given mode is roughly proportional to the coherence length. Furthermore, for our standard eleven step sequences, an edge will be successfully measured (and the corresponding segment "captured") if its phase lies anywhere within $\pm$ 5 steps of the nominal position. Thus the capture range, too, is proportional to the coherence length. This means that we

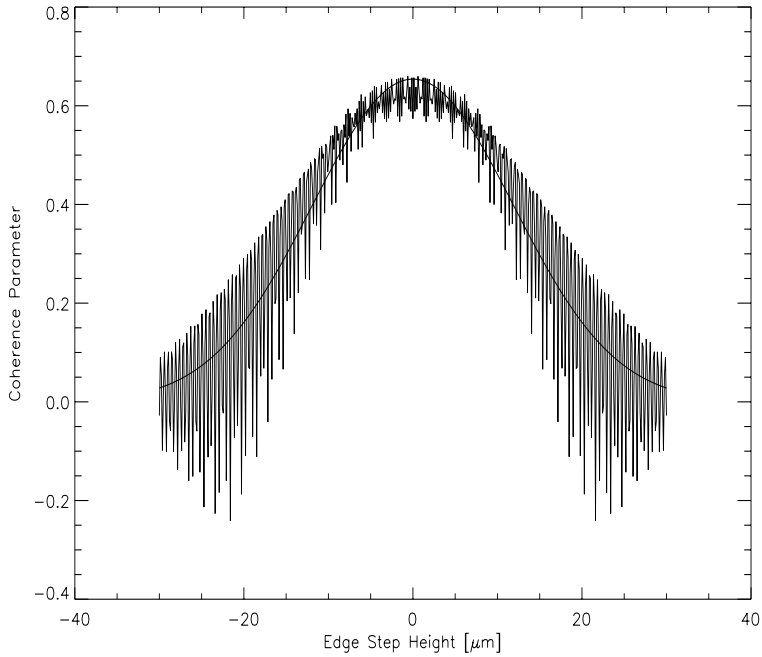

Figure 5. Theoretical curve of coherence parameter vs. edge step height for a filter with central wavelength 891 nm, $\Delta\lambda = 10$ nm, coherence length 40 μm. Smooth curve is the best-fit Gaussian approximation.

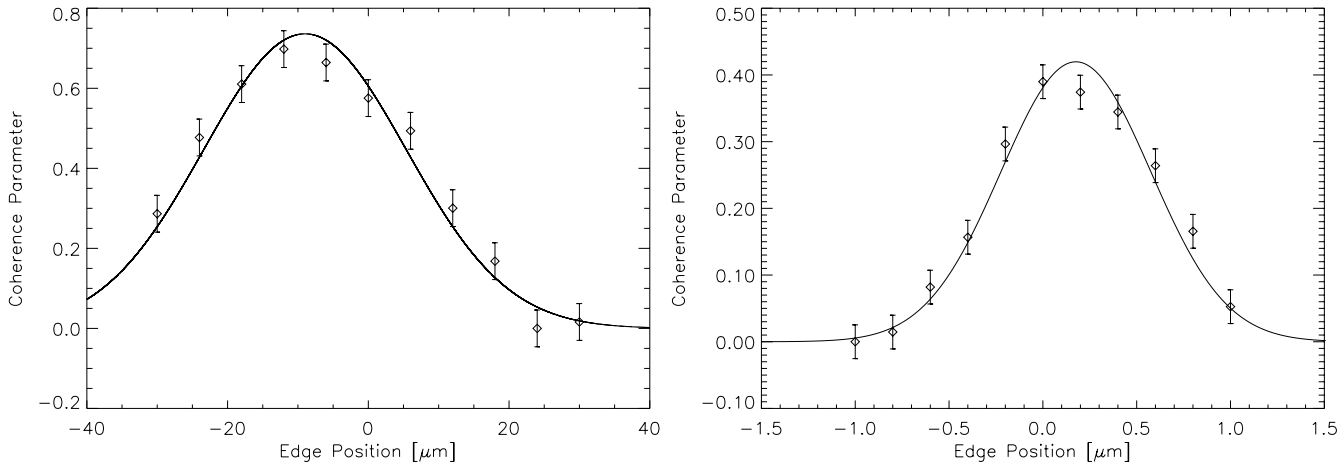

Figure 6. Typical curves of coherence parameter vs. edge position for a filter of coherence length 40 μm ($\Delta\lambda$ =10 nm) (left panel) and for a filter of coherence length 1.2 μm ($\Delta\lambda = 200$ nm) (right panel). The left panel corresponds to the particular sequence of subimages shown in Figure 4.

can cascade the various broadband phasing modes by choosing the capture range of the n+1st mode to be equal to the accuracy of the nth mode. As a result the broadband phasing scheme converges very rapidly, with the total time required increasing only as the log of the initial piston uncertainty.

In addition to the $\Delta\lambda = 10$ nm filter, we use bandwidths of 100 nm or we run unfiltered, in which case the effective bandwidth is about 200 nm. The effective central wavelengths are 891 nm, 870 nm, and 700 nm respectively. The corresponding coherence lengths are $l = 40$, 3.8, and 1.2 μm, the step sizes in the sequences are 6 μm, 0.6 μm, and 0.2 μm, and the capture ranges are $\pm$ 30 μm, $\pm$ 3 μm, and $\pm$ 1 μm, respectively. The largest capture range

of $\pm$ 30 μm associated with the l = 40 μm filter completely eliminates the need for mechanically "pre-phasing" the segments with a hand-held spherometer. Indeed, no spherometry was ever done on Keck 2 prior to successfully phasing the segments. A typical coherence curve for the 700 nm/200 nm filter is shown in Figure 6b.

3.3. PDS Technique

In this algorithm,[10] the signal S is constructed from the sum and difference of inside-of-focus and outside-of-focus images:

$$S = \frac{I_+ - I_-}{I_+ + I_-} \tag{9}$$

[This is the same signal definition used in curvature sensing, although the extraction of phase information from the signal is much different in the present case.] Here I_+ is the image taken a distance ℓ in front of the nominal focus and I_- is taken an equal distance in back of the nominal focus. The image I_- is inverted (rotated by 180 degrees), so that a given ray from the primary mirror hits the same nominal pixel location in both images. Since to first order the sum in the denominator of S is just the uniform intensity with which the pupil is illuminated, the signal S can also be thought of as the difference image $I_+ - I_-$, to within an overall multiplicative constant.

To ensure that the difference image carries useful information on the segment phases, we must satisfy two conditions on the wavelength λ:

(a) The scale of diffraction effects (associated with primary mirror segments) in the image plane should be small compared to the diameter d of a segment mapped onto the image plane, i.e.:

$$\frac{f\lambda}{d} \ll \frac{d\ell}{f} \tag{10}$$

where f is the focal length of the telescope and ℓ is the defocus distance. This is to prevent confusion of the diffraction effects associated with different segments. There is a closely analogous condition in curvature sensing, but with the atmospheric coherence diameter r_0 replacing the segment diameter d.

(b) Diffraction effects associated with the segments should predominate over those associated with the atmosphere, i.e.:

$$r_0(\lambda) \gg d \tag{11}$$

The argument on the left hand side is to emphasize that r_0 here refers to the wavelength of the observations, not to the canonical wavelength of 0.5 μm.

The above conditions can be satisfied for Keck (d = 1.8 m) with a defocus distance ℓ = 0.80 m (out of a focal length f of 250 m), and a wavelength λ of 3.3 μm. The typical Keck coherence diameter of 0.20 m at a wavelength of 0.5 μm is equivalent to an r_0 of 1.9 meters at 3.3 μm. The detector is that of the Near Infrared Camera (NIRC),[15] with 256 x 256 pixels and an image scale of 0.15 arcseconds per pixel.

A mathematical treatment is beyond our scope here, but to get some insight into this method, consider an out-of-focus image of a Keck mirror, perfectly aligned except for segment 13, which has a piston error of $\lambda/8$ (400 nm). This is shown in Figure 7, which was generated numerically by means of a Fast Fourier Transform. Note that, although the algorithm operates on the difference image, this illustration (and also Figure 10) shows only the inside-of-focus image. This avoids the problem that as the phase errors go to zero, the difference image disappears. We include the effects of seeing in the long exposure limit, using the typical Keck value[16] of $r_0(0.5\ \mu m)$ = 20 cm. The dominant feature in this image is well-localized at a position on the detector which has an obvious approximate correspondence to the location of the segment in question in the pupil. For piston errors of this size or smaller, the strength of the feature in the difference image will vary monotonically with the piston error. It follows that multiple piston errors can therefore be extracted from the difference image by straightforward cross-correlation techniques. Because the diffraction pattern of Figure 7 spills over the boundaries corresponding to segment 13 (in Figure 2) and because the linearization effected by the restriction to small piston errors is only approximate, the PDS algorithm does not converge in one step, but rather is an iterative procedure, requiring multiple (typically 5-6) exposures on both star and background.

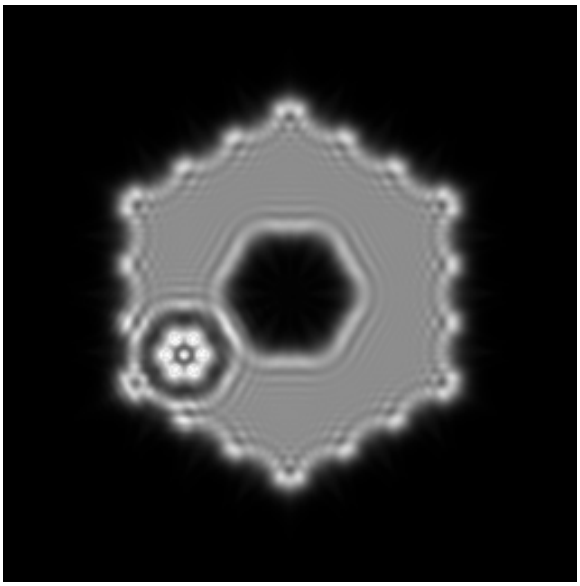

Figure 7. Numerically generated out-of-focus image of the Keck telescope with segment 13 pistoned by $\lambda/8$. Note that the resulting diffraction effects are well-localized at a position that has an obvious correspondence with the position of the segment in the pupil (see Figure 2).

4. RESULTS AND QUANTITATIVE COMPARISON OF THE THREE METHODS

4.1. Narrowband Shack-Hartmann

In practice at Keck, we generally run the narrowband algorithm after the broadband algorithm, to insure that the initial phase errors are sufficiently small. Nevertheless, to parallel the development of Section 3, we present the narrowband results first here. Figure 8 shows a consistency check for the narrowband algorithm in which the algorithm was run eight times at each of two different wavelengths, 651 and 852 nm. The 12 nm RSS difference between the two measurements implies a phasing accuracy of 6 nm (when one takes into account the over-determined nature of the conversion from the 78 edge measurements to the corresponding 36 piston errors).

4.2. Broadband Shack-Hartmann

Figure 9 shows the "before and after" phasing configurations from the first time that the broadband algorithm was ever run on the Keck 2 telescope. In the "before" case, the rms piston errors were 10 μm and individual errors were as large as 30 μm. The most accurate mode of this algorithm was not run this first time, and so the segments were only phased to about 100 nm. In hundreds of subsequent runs the full 30 nm accuracy of the most sensitive mode has been routinely attained.

A narrowband vs. broadband consistency check,[14] similar to that shown in Figure 8, shows that narrowband and broadband edge measurements agree to within 19 nm (RSS), a result which suggests that the claimed 30 nm accuracy of the broadband technique may in fact be conservative.

4.3. Phase Discontinuity Sensing

Figure 10 shows a qualitative consistency check between the broadband Shack-Hartmann technique and phase discontinuity sensing. The telescope was first phased via broadband phasing and then a set of 36 random segment phase errors (200 nm rms) was applied to the primary mirror to produce the out-of-focus image in the left panel of this figure. To produce the right panel the identical set of 36 random segment phases was applied numerically to a perfectly phased mirror, resulting in the simulated image shown. The close correspondence between the real and artificial images of this figure provides immediate confirmation that the Shack-Hartmann and out-of-focus techniques agree to significantly better than 200 nm. Quantitative comparison shows that the two agree to about 60 nm.[10] By repeatedly running the PDS algorithm from different starting points, we infer that the accuracy of this method is 40 nm or better. Since the broadband algorithm to which we compare it has an accuracy of about 30 nm, we would

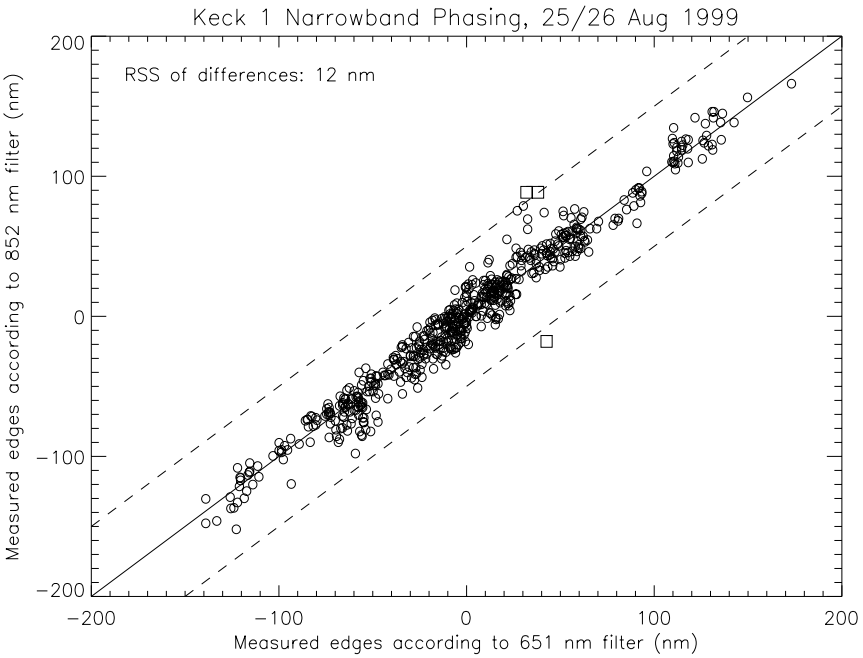

Figure 8. Narrowband edge measurements at two different wavelengths as a consistency check. The 12 nm RSS difference implies a phasing accuracy of 6 nm, which is about what is achieved. Agreement of the individual measurements to within ± 50 nm (dashed lines) is required in order to implement a two-wavelength algorithm with larger capture range.[14] Only three points (squares) out of 624 lie outside of this range.

expect that the rms difference between the two phasing solutions would be equal to the quadrature sum of these errors, or 50 nm. The somewhat larger errors obtained in practice may also include drift in the telescope active control system (since we have only been able to compare the results of the two methods obtained on different nights), or it may reflect a difference in the way that the two algorithms respond to segment aberrations (since the PDS method utilizes a larger fraction of the segment surface).

In Table 1 we present an overall summary of the properties and results of the three methods.

Table 1. Parameters of the Keck Phasing Procedures.

Procedure Name	Narrowband SH	Broadband SH			PDS
Special Instrumentation	yes	yes			no
Pupil Registration	yes	yes			no
Iterative	no	no			yes
Capture Range (μm)	0.100	±30	±3	±1	0.400
Accuracy (nm)	6	1000	100	30	40
Number of Exposures	1	11	11	11	10-12[a]
Execution Time (min)[b]	20	30	30	30	45
Star Magnitude	5	4	5	6	3-4
Central Wavelength (nm)	852	891	870	700	3310
Filter FWHM (nm)	30	10	100	200	63

[a]Includes background exposures. [b]Includes setup time.

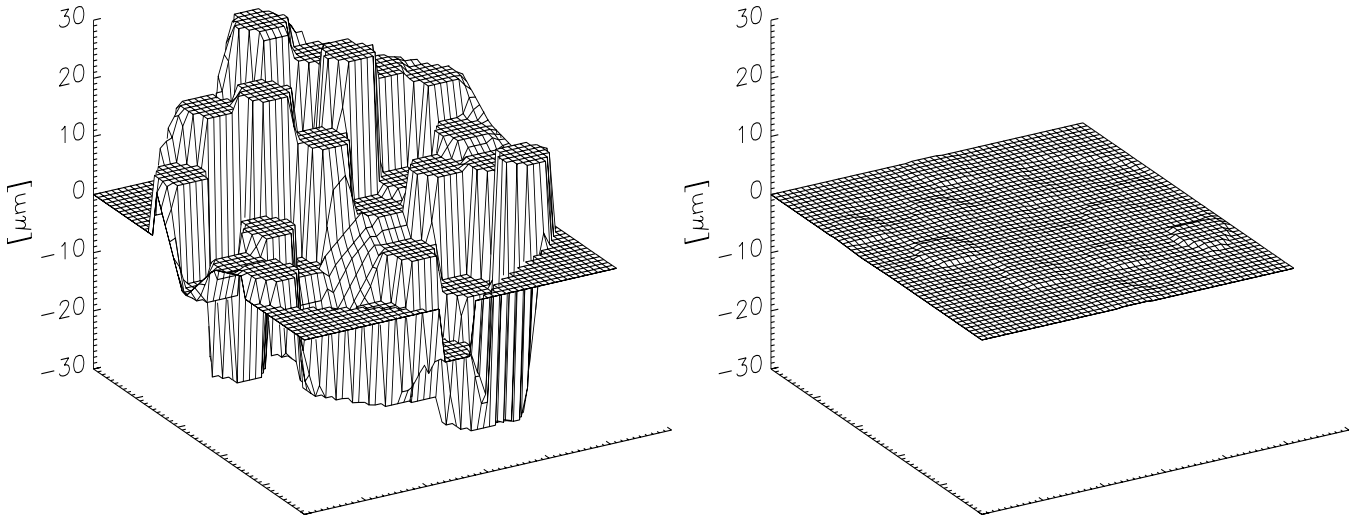

Figure 9. Surface of the Keck 2 primary mirror: (a) before and (b) after phasing. These data represent the first time the procedure was run on this telescope.

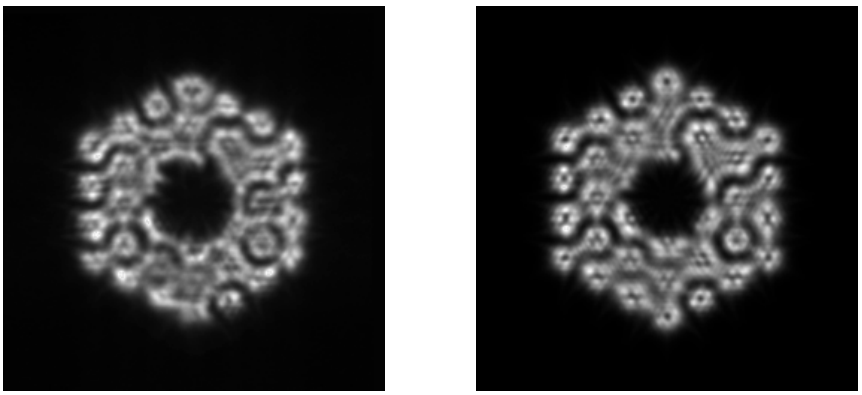

Figure 10. (a) An actual out-of-focus image for a dephased Keck telescope (rms piston error = 200 nm). (b) The same as (a) but from numerically generated data. The close correspondence between the two figures confirms that PDS converges to the same phasing solution as does Shack-Hartmann phasing.

5. APPLICATIONS TO EXTREMELY LARGE TELESCOPES

5.1. Shack-Hartmann Phasing

Shack-Hartmann phasing is a fundamentally parallel algorithm and can therefore in principle accomodate the very large number of segments common to the designs of the extremely large ground-based telescopes of the future. Although the array of microprisms used at Keck would probably be difficult to expand by large factors, we have shown in a series of laboratory measurements that commercially available microlenslet arrays are now of sufficient quality to constitute a viable substitute for microprisms. Thus, for Shack-Hartmann phasing of very large telescopes, the principal concerns have mainly to do with available area on the detector and with computation time.

We can estimate the required CCD size for Shack-Hartmann phasing of the proposed 30 m California Extremely

Large Telescope (CELT) as follows. At Keck the Shack-Hartmann image scale is 6.77 pixels per arcsecond and each subarray corresponding to the diffraction pattern from an intersegment edge is 33 pixels or 4.88 arcseconds on a side. Nearest neighbor patterns are about 60 pixels or 9 arcseconds apart. These numbers are not optimal for phasing a very large telescope, where the CCD would be much more crowded with images. The Keck diffraction patterns actually spill over the boundaries of the subarrays to some extent; nearest neighbors should probably be at least 6 arcseconds apart. Simulations suggest that the Keck image scale is overly generous and a scale of 4 pixels per arcsecond would probably suffice. For the 1098 segment CELT there are about 70 nearest neighbor diffraction patterns across the full aperture phasing image. At the above image scale and nearest neighbor separation this corresponds to 1680 pixels. Thus allowing for appropriate margins, a 2048 by 2048 detector should be adequate. For OWL, a 100 meter telescope with as many as 3600 segments, the required detector would probably be 4096 x 4096.

For CELT the computation time would likely be dominated by the need to invert the very large phasing matrix, nominally 1098 (segments) by 3168 (edge measurements). We have generated the appropriate matrix and inverted it via a Singular Value Decomposition algorithm[17] in about 15 minutes using a 670 MHz Alpha 21264 processor. By the time such a telescope is actually built, we expect the computation time will be negligible.

5.2. Phase Discontinuity Sensing

Central to the PDS method is a series of n "eigenfunctions" consisting of numerically generated out-of-focus images (actually difference images involving outside-of-focus and inside-of-focus images) of a star with a primary that is perfectly phased, except that the j^{th} segment ($j = 1$ to n) has a piston error of $\lambda/8$. These numerical images are generated using two-dimensional Fast Fourier Transforms (FFTs). The required array size for these FFTs grows with and is completely determined by the number of segments in the telescope, as shown in the following argument.

Let A' be the size (in meters) of one side of the aperture array used in the FFT, and let B' be the size (in radians) of one side of the corresponding image or detector array. If the arrays are N x N and the wavelength at which the calculation is performed is λ, then a fundamental relation of discrete Fourier Transforms states that:

$$A'B' = N\lambda \tag{12}$$

Similarly let A be the diameter of the telescope, and let B be the geometrical size of the defocussed image. Clearly we must have $A < A'$ and $B < B'$. In practice there must be a finite margin in both of these inequalities: In general the image scale is set by external considerations; this fixes B' and also sets the grid size in the aperture plane, which in turn establishes A' independent of A. We can relate A and B to N by:

$$AB = \beta N\lambda \tag{13}$$

where β is a factor of order unity, but smaller than one, which takes the above inequalities into account. For PDS as implemented on Keck we have $A = 10$ m, $A' = 18.1$ m, $B = 26.2$ arcsec, $B' = 38.4$ arcsec, $\lambda = 3.3$ μm, and $N = 1024$, although the theoretical images were subsequently binned down to 256 x 256 to match the array size of NIRC. This implies $\beta = 0.38$. We emphasize that because of the relatively modest requirements on the array size set by the small number of Keck segments, there was no attempt to optimize the above parameters. For design purposes now, we assume a still conservative value of $\beta = 0.50$.

The physical condition on B is that the diffraction effects associated with the individual segments cannot overlap too much. We have:

$$B = \frac{\alpha\sqrt{n}\lambda}{d} \tag{14}$$

where n is the total number of segments, d is the circumscribed diameter of a segment (1.8 meters for Keck), and $\alpha > 1$ is a parameter that quantifies the necessary spacing of the segment diffraction patterns. The above Keck parameters give $\alpha = 11.5$. However, as noted above, there was no attempt to optimize the Keck algorithm for arrays or detectors of limited size, so this does not represent a minimal α. From Monte Carlo work we have shown that for Keck a detector that was 4 times smaller would still have worked (although the convergence would have been somewhat slower), but a detector that was 8 times smaller would not have worked. Therefore for design purposes we here assume $\alpha = 3$.

Substituting Eq. (14) into (13) and utilizing $A = d\sqrt{n}$ yields the simple relation:

$$N = \frac{\alpha n}{\beta} \tag{15}$$

i.e. the array size (in each dimension) is simply proportional to the total number of segments. For the nominal parameters used above we have $N = 6n$. Of course in practice this value of N would have to be rounded up to the nearest power of 2. For CELT, its 1098 segments would require arrays of 8192 x 8192; for OWL, a 100 meter telescope with, for example, 3600 Keck-type segments, we would require arrays of 32768 x 32768.

Apart from these large computational arrays (which are only involved in off-line calculations), there appear to be no fundamental problems in extending the PDS approach to extremely large telescopes. The detector arrays can be much smaller than the computational arrays. One only needs several pixels across a segment; a 512 x 512 detector should suffice for either CELT or OWL. Although the images need to be further out-of-focus for larger telescopes, this is largely offset by their increased light gathering power.

ACKNOWLEDGEMENTS

We are grateful to Jerry Nelson for many useful discussions and suggestions concerning these investigations, to Fred Chaffee and Peter Wizinowich of the W.M. Keck Observatory for providing financial support and telescope engineering time, and to Barbara Schaefer and the observing assistants at Keck not only for assisting with, but in many cases carrying out, the observations decribed in this work.

REFERENCES

1. B. Seery and E. Smith, "NASA's Next Generation Space Telescope," in *Space Telescopes and Instruments V*, P. Bely and J. Breckinridge, eds., vol. 3356, pp. 2–13, SPIE, 1998.
2. J. E. Nelson and T. Mast, "Giant optical devices," in *Proceedings of the Backaskog Workshop of Extremely Large Telescopes*, T. Anderson, ed., pp. 1–11, Lund University and ESO, June 1999.
3. R. Gilmozzi, B. Delabre, P. Dierickx, N. Hubin, F. Koch, G. Monnet, M. Quattri, F. Rigaut, and R. Wilson, "The Future of Filled Aperture Telescopes: is a 100 m Feasible?," in Stepp,[18] pp. 778–791.
4. G. A. Chanan, M. Troy, F. G. Dekens, S. Michaels, J. Nelson, T. Mast, and D. Kirkman, "Phasing the mirror segments of the Keck Telescopes: the broadband phasing algorithm," *Applied Optics* **37**, pp. 140–155, Jan. 1998.
5. G. Chanan, G. Djorgovski, A. Gleckler, S. Kulkarni, T. Mast, C. Max, J. Nelson, and P. Wizinowich, "*Adaptive Optics for Keck Observatory*," Keck Observatory Report No. 208, W.M. Keck Observatory, Kamuela HI, Jan. 1996.
6. G. A. Chanan and M. Troy, "Strehl ratio and modulation transfer function for segmented mirror telescopes as functions of segment phase error," *Applied Optics* **38**, pp. 6642–6647, Nov. 1999.
7. M. Troy, G. A. Chanan, E. Sirko, and E. Leffert, "Residual misalignments of the Keck telescope primary mirror segments: classification of modes and implications for adaptive optics," in Stepp,[18] pp. 307–317.
8. G. A. Chanan, J. Nelson, T. Mast, P. Wizinowich, and B. Schaefer, "The W. M. Keck Telescope phasing camera system," in *Instrumentation in Astronomy VIII*, D. L. Crawford and E. R. Craine, eds., vol. 2198, pp. 1139–1150, SPIE, 1994.
9. G. A. Chanan, "Design of the Keck Observatory alignment camera," in *Precision Instrument Design*, T. C. Bristow and A. E. Hatheway, eds., vol. 1036, pp. 59–70, SPIE, 1988.
10. G. A. Chanan, M. Troy, and E. Sirko, "Phase discontinuity sensing: A method for phasing segmented mirrors in the infrared," *Applied Optics* **38**, pp. 704–713, Feb. 1999.
11. C. Roddier and F. Roddier, "New optical testing methods developed at the University of Hawaii: results on ground-based telescopes and Hubble Space Telescope," in *Advanced Optical Manufacturing and Testing II*, V. J. Doherty, ed., vol. 1531, pp. 37–43, SPIE, 1991.
12. F. Roddier, "Curvature sensing and compensation: a new concept in adaptive optics," *Applied Optics* **27**, pp. 1223–1225, Apr. 1988.
13. F. Roddier, "Wavefront sensing and the irradiance transport equation," *Applied Optics* **29**, pp. 1402–1403, Apr. 1990.
14. G. A. Chanan, C. Ohara, and M. Troy, "Phasing the mirror segments of the Keck telescopes II: The Narrowband Phasing Algorithm," (preprint).
15. K. Matthews and B. T. Soifer, "The near infrared camera on the W. M. Keck Telescope," in *Infrared Astronomy with Arrays: the Next Generation*, I. S. McLean, ed., pp. 239–246, Dordrecht: Kluwer Academic Publishers, Boston, 1994.
16. J. E. Nelson and P. R. Gillingham, "Overview of the performance of the W. M. Keck Observatory," in *Advanced Technology Optical Telescopes V*, L. M. Stepp, ed., vol. 2199, pp. 92–93, SPIE, 1994.
17. W. Press, B. Flannery, S. Teukolsky, and W. Vetterling, *Numerical Recipes: The Art of Scientific Computing*, pp. 52-64, 502-515. Cambridge University Press, New York, 1989.
18. L. M. Stepp, ed., *Advanced Technology Optical/IR Telescopes VI*, vol. 3352, SPIE, 1998.